REPORT DOCUMENTATION PAGE

OMB No. 0704-0188

1. REPORT DATE *(DD-MM-YYYY)*	2. REPORT TYPE Final Technical Report	3. DATES COVERED (From – To) 11 April 2003 – 30 June 2006

4. TITLE AND SUBTITLE Structural Health Monitoring for Heterogeneous Systems	5a. CONTRACT NUMBER
	5b. GRANT NUMBER F49620-03-1-0174
	5c. PROGRAM ELEMENT NUMBER

6. AUTHOR(S) Dr. Aditi Chattopadhyay	5d. PROJECT NUMBER
	5e. TASK NUMBER
	5f. WORK UNIT NUMBER

7. PERFORMING ORGANIZATION NAME(S) AND ADDRESS(ES) Arizona State University Department of Mechanical and Aerospace Engineering Tempe AZ 85287-6106	8. PERFORMING ORGANIZATION REPORT NUMBER

9. SPONSORING/MONITORING AGENCY NAME(S) AND ADDRESS(ES) Air Force Office of Scientific Research (AFOSR) 875 N. Arlington St., Rm. 3112 Arlington, VA 22203 Dr Victor Giurgiutiu/NA	10. SPONSOR/MONITOR'S ACRONYM(S) AFOSR
	11. SPONSORING/MONITORING AGENCY REPORT NUMBER AFRL-SR-AR-TR-07-0121

12. DISTRIBUTION AVAILABILITY STATEMENT

DISTRIBUTION A: Approved for public release. Distribution is unlimited.

13. SUPPLEMENTARY NOTES

A hierarchical framework has been developed for damage characterization, detection and quantification in composite laminates. The procedure includes accurate analysis, optimal sensor placement algorithm and advanced signal processing technique. A refined global/local laminate analysis technique, including fully coupled electro-mechanical constitutive relations, has been used for predicting the dynamic response of composite laminates in the presence of delaminations. The methodology accounts for the nonlinear "breathing phenomenon" or sublaminate contacts during vibration. Damage identification is conducted using elastic waves and miniaturized piezoelectric sensors. A new design methodology for optimal sensor placement has been developed based on the requirements of sensing certainty and sensor density. An analytical method has been developed to model the material attenuation of the composite medium to formulate a relationship between sensing region, sensor observation angle, fiber orientation, and damage size. A signal processing technique based on the matching pursuit decomposition has been further extended to extract newly generated spectral components due to the nonlinearity in the received signal. Time-of-flight analysis has been performed on decomposed components of transient datasets to quantify defect. An advanced machine-learning based classifier, known as Support Vector Machines, has also been developed to detect and classify the signature characteristics due to the presence of various types of defects like delaminations, drilled holes, notches, saw-cut, etc., such that the state of the structure can be assessed. Experiments have been conducted using a variety of nondestructive evaluation (NDE) techniques, including pulse echo thermography, to validate the developed methodologies.

Standard Form 298 (Rev. 8-98)
Prescribed by ANSI Std Z39-18

15. SUBJECT TERMS

STRUCTURAL HEALTH MONITORING FOR HETEROGENEOUS SYSTEMS

Final Report
Period Covered: April 11, 2003 – June 30, 2006
AFOSR Grant Number: F496200310174
Technical Monitor: Dr. Clark Allred

Principal Investigator: Aditi Chattopadhyay
Department of Mechanical and Aerospace Engineering
Arizona State University
Tempe, Arizona 85287-6106

20070417192

STRUCTURAL HEALTH MONITORING FOR HETEROGENEOUS SYSTEMS

A hierarchical framework has been developed for damage characterization, detection and quantification in composite laminates. The procedure includes accurate analysis, optimal sensor placement algorithm and advanced signal processing technique. A refined global/local laminate analysis technique, including fully coupled electro-mechanical constitutive relations, has been used for predicting the dynamic response of composite laminates in the presence of delaminations. The methodology accounts for the nonlinear "breathing phenomenon" or sublaminate contacts during vibration. Damage identification is conducted using elastic waves and miniaturized piezoelectric sensors. A new design methodology for optimal sensor placement has been developed based on the requirements of sensing certainty and sensor density. An analytical method has been developed to model the material attenuation of the composite medium to formulate a relationship between sensing region, sensor observation angle, fiber orientation, and damage size. A signal processing technique based on the matching pursuit decomposition has been further extended to extract newly generated spectral components due to the nonlinearity in the received signal. Time-of-flight analysis has been performed on decomposed components of transient datasets to quantify defect. An advanced machine-learning based classifier, known as Support Vector Machines, has also been developed to detect and classify the signature characteristics due to the presence of various types of defects like delaminations, drilled holes, notches, saw-cut, etc., such that the state of the structure can be

assessed. Experiments have been conducted using a variety of nondestructive evaluation (NDE)

techniques, including pulse echo thermography, to validate the developed methodologies.

Objectives

A comprehensive research on characterization, detection and estimation of seeded delaminations in composites has been conducted. A hierarchical sensor integrated framework has been developed, combining simulation, wave propagation based detection, signal processing and classification techniques. Following are the principle objectives of this research.

1. *Wave propagation in heterogeneous media and optimal sensor placement based on the concept of sensing region and detection criteria.* A two-dimensional design methodology associated with optimal placement of sensor sets has been developed based on the characterization of sensor sensing region and performance. Convergence of sensing regions with the required level of inspection accuracy leads to the certainty region of detectability, implying that perturbations caused by damage in that region with severity greater than the threshold value can be detected.

2. *Hierarchical Inspection Method.* A "local energy based" inspection method has been developd taking into account both the "local" and "global" effects on the structural response of composite structures.

3. *Material attenuation and its effect on damage detection and sensor placement.* A model for predicting the influence of the combined effects of fiber angle and observation angle on attenuation coefficient of composite laminate has been developed. The goal is to achieve a thorough understanding on the relationship between sensing region, observation angle, fiber orientation, and damage size.

4. *Time-frequency based damage detection techniques.* A methodology for localized analysis of waveforms obtained from damaged structures has been developed using the Matching Pursuit Decomposition (MPD) technique and time-frequency representations (TFRs) with a broader view of damage quantification.

5. *Signal processing techniques.* Suitable signal processing techniques, based on the MPD, has been developed to investigate the vibration attributes of delaminations in composites. The

present work concentrates on the applicability of the MPD technique to extract some feature components of "multiple-harmonic" vibration of elastic bodies.

6. *Damage classification.* An automated method for classifying sensor signals, collected from different types of damaged coupons, has been developed to enable the detection and diagnosis of various forms of damage on composite structures using Support Vector Machines (SVMs), which are an advanced form of classification method from the field of machine learning.

Summary of Research Efforts

A comprehensive framework has been developed including damage characterization in composites, advanced signal processing for damage detection, and optimal sensor placement. A methodology has been developed to achieve optimal sensor placement and convergent descriptions of possible damages in the presence of noise through characterization of sensor/host structure coupling, sensing capability and sensor sensitivity. A local energy based inspection method has also been developed by formulating a damage indicator based on local energy perturbations due to possible presence of damage. Through the integration of the developed sensor network and identification technique, damage can be detected through local energy effects of individual sensors to that of the overall responses of the distributed sensors. The present procedure also incorporates the effects of the transducer-structure bonding and the characterization of the sensors sensing region in the presence of system noise (both structural and electronic). The optimal placement of the transducers is subjected to the minimum overlap criteria such that the sensing regions of the sensor set provide sufficient spatial coverage, and relevant damage information leads to convergence even in the presence of noise, based on the state of excitation and concurrent signal-to-noise ratio. Damage identification has been conducted using elastic waves and miniaturized piezoelectric sensors. A refined global/local

3

laminate analysis technique has been used for the characterization of damage in composites. The efficient and accurate structural analysis uses both higher order and layerwise displacement field formulations and fully coupled electro-mechanical constitutive relations. Results indicate that the presence of delamination in composites significantly affects the energy contribution of individual sensors, depending on their relative positions with respect to damage zones. Characterization studies have been conducted to obtain the sensor parameters which are then used in the identification procedure to detect structural damage. A fundamental investigation into fiber/matrix wave propagation and scattering has been conducted. An analytical method has been developed to model the material attenuation of the composite medium to formulate a relationship between sensing region, sensor observation angle, fiber orientation, and damage size. A hierarchical approach has been adopted to improve the monitoring technique for further quantification of delaminations patterns. In the current effort, a Matching Pursuit Decomposition (MPD) algorithm has been developed for detection and localization of seeded delamination in composite structures. A characterization of sensor signals has been conducted to interpret the influence of delamination in composite plates using the MPD technique. This has been accomplished by decomposing the signal in terms of wave-based dictionary elements and finally utilizing the time-of-flight information of these individual decomposed components of transient datasets to determine the location and size of the delamination. The developed signal processing technique based on the MPD has been further extended to extract newly generated spectral components due to the nonlinearity in the received signal. An advanced machine-learning based classifier, known as Support Vector Machines, has also been developed to detect and classify the signature characteristics due to the presence of various types of defects like delaminations, drilled holes, notches, saw-cut etc. in composite structures so that the status of the structure can be ascertained. Experiments have been conducted using a variety of nondestructive evaluation

4

(NDE) techniques, including pulse echo technique, thermography, to visualize the presence of damage.

Accomplishments

1. Optimal Transducer Placement Technique

A design methodology for optimal sensor sets is developed based on the characterization of sensors' sensing regions and performance. Convergence of sensing regions with the required level of inspection accuracy leads to the certainty region of detectability, implying that perturbations caused by the damage in the corresponding region with severity greater than the threshold value can be detected. To quantify such sensing regions, an experimental characterization is first conducted and then the sensing region is determined using the corresponding sensor response. For a surface mounted sensor-actuator pair, the transfer function can be expressed as follows.

$$\frac{V_S(t)}{V_A(t)} = \left[T_{em} T_{me} \right] \exp(-\alpha(f) R_{AS})$$

(1)

where $V_A(t)$ and $V_S(t)$ are the excitation and the sensing response, respectively and T_{em} and T_{me} are the actuator and sensor transfer functions, respectively. The parameter $\alpha(f)$ is the attenuation coefficient at excitation frequency (f) and R_{AS} is the distance between the actuator and the sensor. When PZT-1 acts as an actuator (Fig. 1), the energy ratio of the sensor signals over the time interval can be related as follows.

$$\frac{\sum_{n=1}^{N-1} E^n_{s1PZT1}}{\sum_{n=1}^{N-1} E^n_{s2PZT1}} = \left(\frac{T_{me1}}{T_{me2}} \right)^2$$

(2)

where $\sum_{n=1}^{N-1} E^n_{s1_{PZT1}}$ & $\sum_{n=1}^{N-1} E^n_{s2_{PZT1}}$ represent the energy of Sensor-1 signal and Sensor-2 signal, respectively. If PZT-2 acts as an actuator, R_{AS1} (R_{AS2}) being the distance between PZT-2 and Sensor-1 (Sensor-2), the signal attenuation coefficient is then given by

$$\alpha(f) = -\frac{1}{2abs\left(R_{AS1} - R_{AS2}\right)} \ln\left(\frac{\sum_{n=1}^{N-1} E^n_{s1_{PZT2}}}{\sum_{n=1}^{N-1} E^n_{s2_{PZT2}}} * \frac{\sum_{n=1}^{N-1} E^n_{s2_{PZT1}}}{\sum_{n=1}^{N-1} E^n_{s1_{PZT1}}} \right)$$
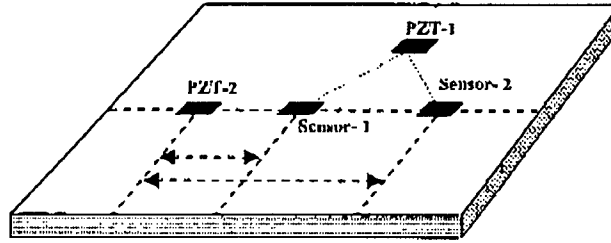
(3)

Fig. 1 Experimental setup for sensor characterization

The detection performance of the sensor is evaluated based on the generalized likelihood ratio test (GLRT). In GLRT process, the maximum likelihood estimates (MLE) of the unknown parameters are first determined and thereafter the maximum likelihood ratio is calculated corresponding to the MLE of the parameters in the test statistics ($L(x)$). In general, the GLRT decides H_1 when,

$$L(x) = \frac{p\left(x; \hat{\theta}, H_1\right)}{p\left(x; H_0\right)} = \max_{\hat{\theta}} \frac{p\left(x; \hat{\theta}, H_1\right)}{p\left(x; H_0\right)} > \gamma$$

(4)

where γ is the threshold parameter. The significance of Eq. (4) is that the developed test statistics maximizes the likelihood ratio over the estimated parameter $\hat{\theta}$ and hypothesis is assumed to be true only when the likelihood ratio is greater than the threshold γ. Assuming that

the noise variance σ^2 and f_0 is known, the present analysis boils down to a narrowband detection process that decides on the presence of the sinusoid with amplitude and phase as unknown parameters. Hence Eq. (4) can be rewritten as,

$$L(x) = \frac{\frac{1}{\left(2\pi\sigma^2\right)^{\frac{N}{2}}} \exp\left[-\frac{1}{2\sigma^2} \sum_{n=0}^{N-1} \left(x(n) - \hat{A}\cos\left(2\pi f_0 n + \hat{\phi}\right)\right)^2\right]}{\frac{1}{\left(2\pi\sigma^2\right)^{\frac{N}{2}}} \exp\left[-\frac{1}{2\sigma^2} \sum_{n=0}^{N-1} x^2(n)\right]} > \gamma \tag{5}$$

where $\hat{A}$ and $\hat{\phi}$ are the MLE of the amplitude and phase. Following some mathematical manipulations, the decision criteria of the modified test statistics $(T(x))$ can be expressed as,

$$T(x) = \frac{1}{N}\left|\sum_{n=0}^{N-1} x(n)e^{-j2\pi f_0 n}\right|^2 > V_{th}^2 \tag{6}$$

where V_{th} is the new threshold value, N denotes the total number of observed data points and j is imaginary unit. Eq. (6) states that a signal can be present if the peak value of the periodogram exceeds a specific threshold, evaluated at the frequency of excitation (f_0). The threshold value physically means the power corresponding to certain frequency, for a given sensor signal ($x(n)$). The detection performance of the sensor is evaluated based on the generalized likelihood ratio test (GLRT) approach, and can be expressed as follows.

$$P_{fa} = \exp\left(-\frac{V_{th}^2}{\sigma^2}\right) \tag{7}$$

where P_{fa} and σ^2 denote the probability of false alarm and known variance for a specific probability value obtained from the noise data, respectively..

1.1 Effective Sensitivity Region

It is worthwhile mentioning that the perturbation caused by the presence of the defects in a certain region that results in an effect with severity greater than the specified threshold value, at the receiver end, is detectable. Such perturbation is then characterized by the following relation,

$$V_{xy} \exp\left(-\alpha R_{xys}\right) = V_s \tag{8}$$

and to satisfy the detection criteria, the following must hold good.

$$V_s \geq V_{th} \tag{9}$$

where V_{xy} is the intensity of the source of the perturbation at any surface point (x, y), V_s is the intensity at the receiver node, V_{th} is the threshold value, and R_{xys} is the absolute distance between the point (x, y) and the sensor node. The sensing region can be further derived using Eq. (8) and Eq. (9).

The sensing region is defined as the distance corresponding to the generated perturbation that would result in a sensor response greater than or equal to the threshold voltage. The distribution of such possible perturbed sources is shown in Fig. 2. Based on the analysis of the experimental data, the sensing radius (R_s) is calculated to be 0.052 m (Fig. 3), with D=0.1 m, R_{as1}=0.05 m, R_{as2}=0.15 m (Fig. 2) and a threshold voltage of 1.1364×10^{-2} v for a P_{fa} of 10^{-4}. The optimal placement of sensors is then determined by satisfying the minimum overlap criteria (Fig. 4), for the specified plate structure as shown in Fig. 5. The surface area is divided into small grids and the shaded region (indicated "1", Fig. 5) shows the detectable region. A simple geometric relation can find the centers of the circles forming an equilateral triangle with a spacing of $\sqrt{3} \, R_s$ and the angles (α, β, γ) equal to $\pi/3$.
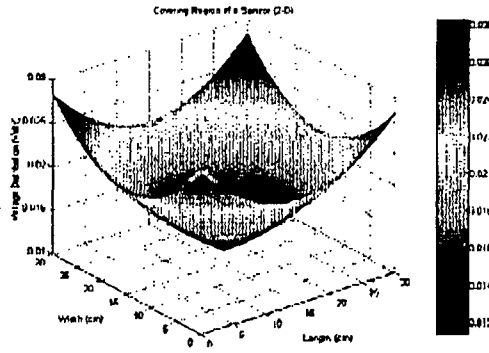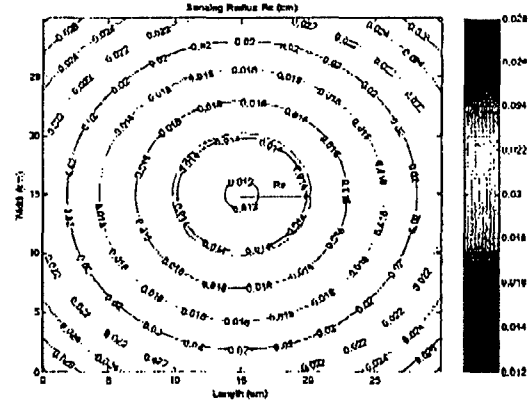
8

Fig. 2: Sensor voltage distribution.

Fig. 3: Estimated sensing radius for required inspection and threshold values.
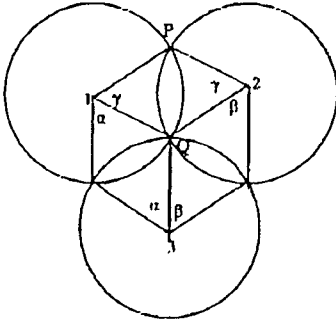

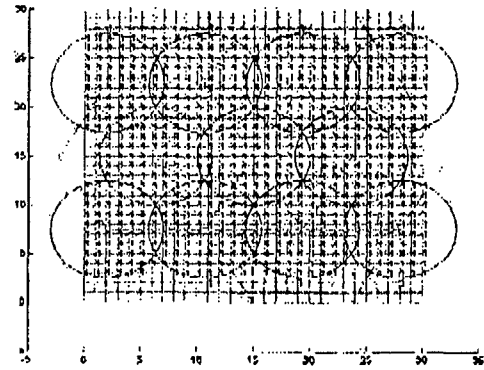Fig.4: Illustration of sensing intersections.

Fig. 5: Optimal sensor placement for a square plate.

The developed "local energy based inspection" method uses local quantification of the energy. The damage indicator, based on the change in energy contribution (Δ) as in Eq. (12), takes into account the local physical effects (Eq. (10)), compared to the overall performance (Eq. (11)) of all the sensors, spatially distributed over the entire structure. Here E_{iH} (E_{iD}) and $E_{avg(H)}$ ($E_{avg(D)}$) represents the energy of the ith sensor signal and average energy over all the sensors for the healthy (delaminated) structure.

$$E_{local} = \left(\frac{E_{iH}}{E_{iD}} \right)$$

(10)

9

$$E_{global} = \left(\frac{E_{avg(H)}}{E_{avg(D)}} \right)$$
(11)

$$\Delta = 1 - \left(\frac{E_{iH}}{E_{iD}} \right) \left(\frac{E_{avg(D)}}{E_{avg(H)}} \right)$$
(12)

Results are presented for a $[0^0/90^0]_{4S}$ Graphite/Epoxy laminated plate with surface mounted actuator and sensors. The length of the square plate is 0.3 m, and the total thickness $h=2.81\times10^{-3}$ m. The plate is clamped at two edges and the other edges are kept free. The locations of the transducers are shown in Fig. 6. The same transducers are used as actuator/sensor. The damages are a pair of seeded delamination with a dimension of 0.04×0.045 m at the 4th or 7th ply interfaces (with respect to the mid plane) and located at a distance of 0.02 m from the edges (Fig. 6).
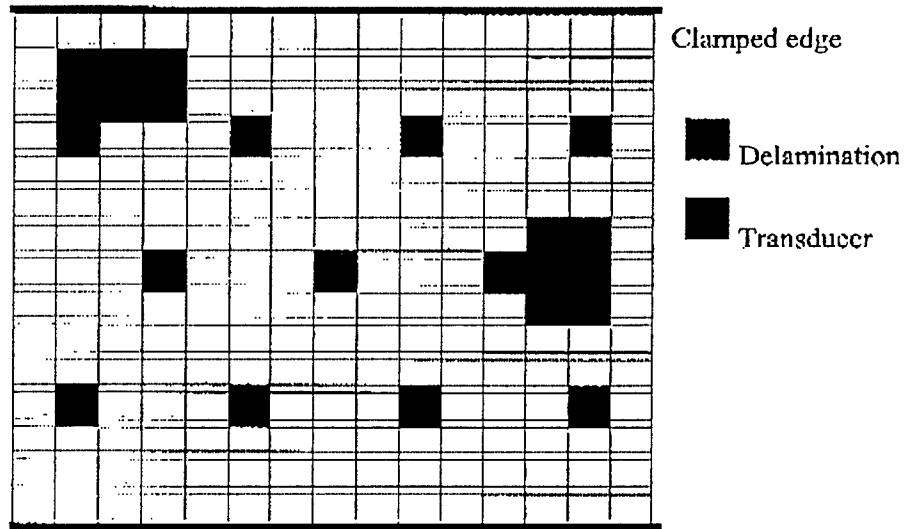
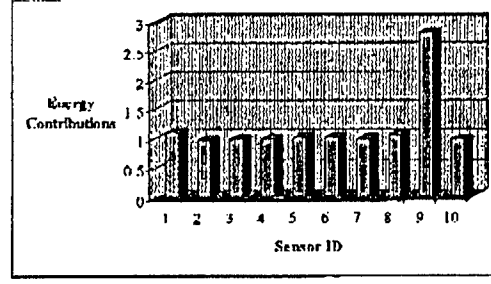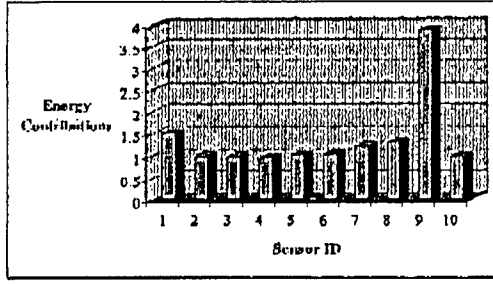Fig. 6: Illustration of surface mounted transducers and delaminations.

Fig.7: Local effects (healthy and 4th ply delamination).   Fig.8: Local effects (healthy and 7th ply delamination).

The first set of results (Figs. 7 and 8) show that the local effects of Sensors 1 and 9 are significantly above the global energy contribution [$E_{global}(l_4)$=1.1532 $E_{global}(l_7)$= 1.0333]. Such effects are more dominant when the positions of Sensors 7 and 8 are relatively closer to the damaged prone region and are more pronounced for delaminations located closer to the mid-plane. When the delaminations are closer to the free surface of the plate (such as 7th ply delamination), the stiffness of the delaminated plate is comparable to the healthy plate. Therefore the difference in strains between a healthy and delaminated plate is small.
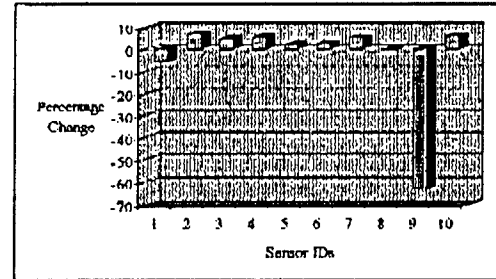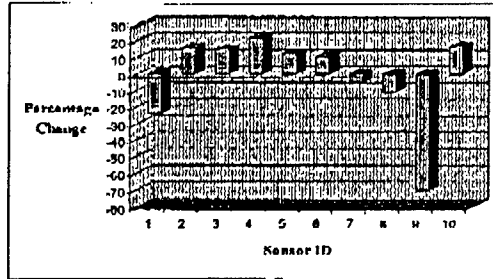

Fig. 9: Change in energy contributions (4th ply   Fig. 10: Change in energy contributions (7th ply
delamination).   delamination).

The second set of results (Figs. 9 and 10) present the variation of energy contributions with respect to individual sensors. This change is visible for all the sensors around the delaminated region. Hence it is possible to locate the damage prone region based on the global coordinates of sensors (sensor IDs).

2. Attenuation Behavior/Elastic Wave Propagation

To estimate energy scattering of wave propagation in fiber-reinforced composite laminates, a plane time-harmonic elastic wave is considered. For a given frequency ω, the plane wave propagating in the r direction can be expressed as (Fig. 11),
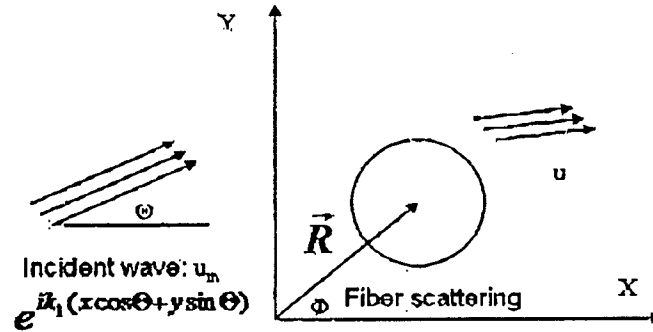

Figure 11 Illustration of wave scattering due to a fiber.

$$u_k(r,\omega) = U_k(\omega)e^{i(Kr - \omega t)} = U_k(\omega)e^{-\alpha r}e^{i(\frac{r}{c(\omega)} - \omega t)} \tag{13}$$

where u_k is the displacement component in the k direction, and $U_k(\omega)$ is the corresponding amplitude factor, typically dependent on the operating frequency and the boundary condition. The quantity K is the complex wave number, α the attenuation factor ($\alpha(\omega) \geq 0$), and $c(\omega)$ is the effective wave velocity. Note that i is the imaginary unit.

The presence of the fiber-matrix interface in the volume element gives rise to wave scattering which diminishes the intensity of the incident wave, which can be expressed in the following form,

$$\langle I(r,\omega)\rangle = \langle I_o(r,\omega)\rangle e^{-\alpha r} \tag{14}$$

12

where $\langle I(r,\omega)\rangle$ denotes the incident wave intensity, and $\langle I_0(r,\omega)\rangle$ is the corresponding amplitude which is proportional to the square of the displacement amplitude per unit area. Therefore, the variation of the wave intensity in the r direction is,

$$\frac{\partial\langle I(r,\omega)\rangle}{\partial r} = -2\alpha\langle I(r,\omega)\rangle \tag{15}$$

To quantify wave scattering in fiber-reinforced composites, a representative control volume element has been defined in Fig. 13. Considering the conservation of energy in the control volume element, the total energy dissipated by the scattering wave can be expressed as,

$$\langle P_t^{SC}\rangle = \langle I(r,\omega)\rangle S - \left[\langle I(r,\omega)\rangle + \frac{\partial\langle I(r,\omega)\rangle}{\partial r}dr\right]S \tag{16}$$

where S is the surface of the control volume element, and $\langle P_t^{SC}\rangle$ represents the total time averaged energy of the scattered waves induced by the fiber-matrix interfacial interaction in the control volume. Note that a dilute interaction is assumed, which implies that only primary scattering is considered. It is important to mention that in most practical problems, dilute solutions are considered adequate.

2.1 Single Fiber Scattering Formulation

It has been shown that the piezoelectric shear transducers will mainly excite shear waves. Therefore, an anti-plane shear wave from a single fiber is considered. The total energy flow per unit area for the scattered field is the time average of the effective flux over any surface assigned to be the area enclosing the cylinder (fiber) of unit length (Fig. 12). Then the scattered energy for a single fiber of unit length can be expressed as
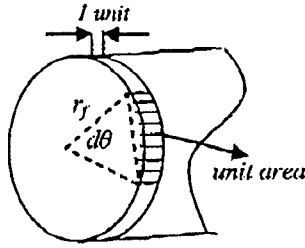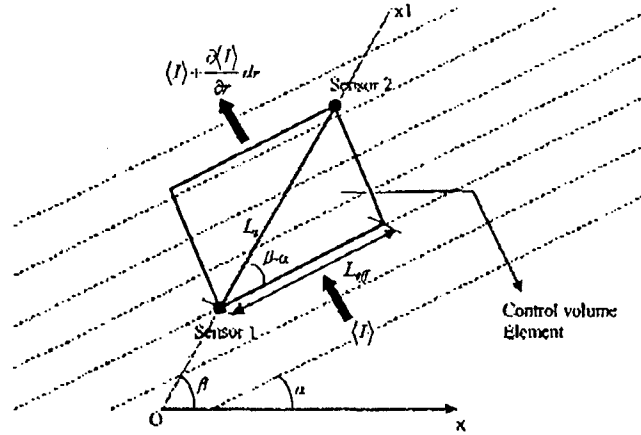
Fig. 12. Single fiber cross section.

Fig. 13. Fiber-reinforced composite and representative volume element.

$$\left\langle P_f^{SC} \right\rangle_{UA} = \frac{\omega}{2} \operatorname{Im} \int_S \mu_1 u^{SC} \frac{\partial u^{SC}}{\partial n} \left(2\pi r_f d\theta \right)$$

(17)

where u^{SC} is the scattered wave, μ_1 be the shear modulus of the matrix, r_f the fiber radius and $\left\langle P_f^{SC} \right\rangle_{UA}$ is the energy flow per unit area of a single fiber (Fig. 12) for the scattered field. Note that this quantity describes the energy scattered in all directions and thus the amount of the energy lost by the incident wave at the cost of it's interaction with the unit area of the fiber.

Therefore the total scattered energy ($\left\langle P_f^{SC} \right\rangle$), for a single fiber with the effective length (L_{eff}), can be expressed as,

$$\left\langle P_f^{SC} \right\rangle = \left\langle P_f^{SC} \right\rangle_{UA} L_{eff}$$

(18)

Let $\sigma^0(\omega)$ be the total scattering cross-section for perfectly bonded fiber. Then $\sigma^0(\omega)$ can be defined as the total scattered energy divided by the incident wave intensity. That is,

14

$$\sigma^0(\omega) = \frac{\left\langle P_f^{sc} \right\rangle}{\langle I \rangle} \tag{19}$$

2.2 Multiple-Fiber Scattering Formulation

Since the mutual interaction or multiple effects among individual fibers have been neglected in the present study, the individual fibers can be regarded as independent of each other. In the control volume element it is assumed that all identical fibers are aligned in the matrix such that there are N_{eff} fibers per unit area in the plane perpendicular to the fiber axis and hence the total scattering energy,

$$\left\langle P_t^{sc} \right\rangle \cong N_{eff} \left\langle P_f^{sc} \right\rangle_{UA} L_{eff} \tag{20}$$

When the wave travels along the O-X1 direction that makes an angle β with the O-X, the respective volume element is exactly identical with that shown in Fig. 13. For convenience each variable is identified with a suffix 'β' for this specific case. Hence the effective fiber length and the attenuation coefficient (α_β^0) computed respectively for this certain angle as,

$$L_{eff} = L_s \cos(\beta - \alpha) \tag{21}$$

$$\alpha_\beta^0 = \frac{1}{2} \left(\frac{N_{eff}}{V_c} \right) L_s \frac{\left\langle P_f^{sc} \right\rangle_{UA}}{\langle I \rangle_\beta} \cos(\beta - \alpha) \tag{22}$$

where L_s is the distance between the two measuring points (the distance between the sensors in the present case), α denotes the angle of ply orientation, and V_c is the control volume. This

relation shows that, the effective attenuation coefficient is influenced by the cumulative effect of the resultant scattered energy from all layers and the different angle $(\beta - \alpha)$.

To obtain the loss due to the wave scattering for composite laminates, by considering a total k layers, the total scattered energy can be expressed as follows,

$$\left\langle P_t^{sc} \right\rangle_\beta^k = N_{eff}^k \left\langle P_f^{sc} \right\rangle^k \tag{23}$$

where $\left\langle P_f^{sc} \right\rangle^k$ is the energy scattering of the layer k, and can be obtained from Eqs. (20) and (21),

$$\left\langle P_f^{sc} \right\rangle^k = L_s \sum_{j=1}^{k} \left(\left\langle P_f^{sc} \right\rangle_{UA,j} \cos\left(\beta - \alpha_j\right) \right) \tag{24}$$

It is important to mention that the current approach to sum over the scattering energy over individual layers would be entirely adequate because the final expression is determined using sample equations which stem from energy considerations. Eq. (12), can be rewritten in terms of individual layer contribution,

$$\left\langle P_f^{sc} \right\rangle^k = L_s \left\langle P_f^{sc} \right\rangle_{UA,k} \left\{ \left(\frac{\left\langle P_f^{sc} \right\rangle_{UA,1}}{\left\langle P_f^{sc} \right\rangle_{UA,k}} \cos(\beta - \alpha_1) \right) + \left(\frac{\left\langle P_f^{sc} \right\rangle_{UA,2}}{\left\langle P_f^{sc} \right\rangle_{UA,k}} \cos(\beta - \alpha_2) \right) + K \ K \ + \cos(\beta - \alpha_k) \right\} \tag{25}$$

To simplify the analysis, the energy flow in a control volume element with three layers has been considered (Fig. 14). Considering that no energy can be created or destroyed within the control

volume, the input energy of the jth layer must be equal to the input energy of the $(j+1)^{th}$ layer plus the energy carried away by the scattered wave in the jth layer. This can be expressed as,
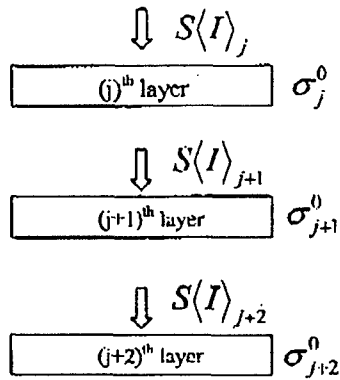

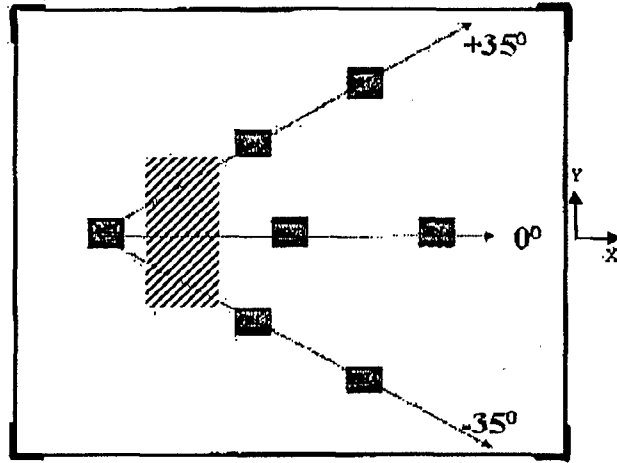Fig.14. Layerwise energy flow in composite laminates.

Figure 15. Experimental setup and plate geometry.

$$\langle I \rangle^{j} S - \langle I \rangle^{j+1} S = \left\langle P_{f}^{sc} \right\rangle^{j}$$

(26)

Combination of Eqs. (26) and (19), would result in,

$$\frac{\left\langle P^{sc} \right\rangle_{j}}{\left\langle P^{sc} \right\rangle_{j+1}} = C_{j,j+1} = \frac{1}{\sigma_{j+1}^{0} \left(\frac{1}{\sigma_{j}^{0}} - 1 \right)}$$

(27)

Therefore Eq. (25), can be rewritten for the k layers as follows,

$$\left\langle P_{f}^{sc} \right\rangle^{k} = L_{s} \left\langle P_{f}^{sc} \right\rangle_{UA,k} \left\{ \left(C_{1,k} \cos(\beta - \alpha_{1}) \right) + \left(C_{2,k} \cos(\beta - \alpha_{2}) \right) + K\ K\ + \cos(\beta - \alpha_{k}) \right\}$$

(28)

It is possible to estimate these parameters ($C_{1,k}$, $C_{2,k}$, ...) through numerical calculations for a specific composite with some known parameters like elastic constant, fiber radius and incident wave.

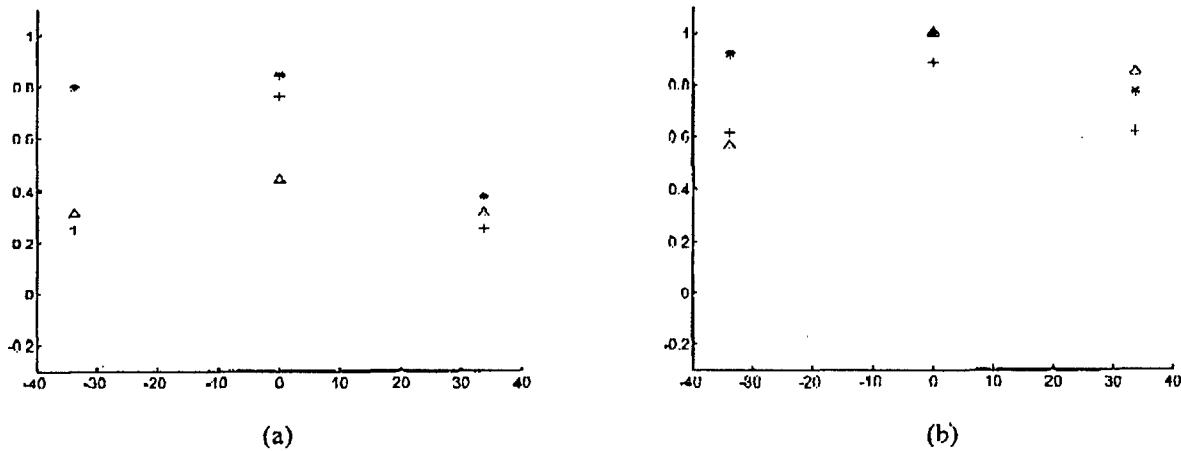(a)   (b)

Fig. 16. Normalized attenuation with varying observation angle (-34/0/34 deg.) (a) 0/0 (b) 0/90 stacking sequence (Comparison of simulation (+), experimental (*) and theoretical (Δ) results for healthy case)

The dependency of the normalized attenuation coefficient on observation angle (β) is shown in Fig.16a-16b. It is seen from Fig.16a-16b that the variation of the normalized attenuation is almost symmetrical about $\beta = 0$ deg. Similar patterns are observed for both 0/0 and 0/90 stacking sequences. For normal incidence, the pattern shows that the maximum value of the attenuation coefficient always occurs at $\beta = 0$ for a given stacking sequence. However for a fixed observation angle, the value of the normalized attenuation coefficient is a maximum for a 0/90 stacking sequence. In this context, it is important to note that Fig.16a-16b has some relevance to wave based quantitative nondestructive evaluation for optimally locating the sensor in order to efficiently intercept the scattered signal.

3. Time Frequency Based Damage Detection and Quantification

A distinct feature of nonlinear systems is the frequency component from the generated harmonic response that is different from the harmonic excitation frequency. When a localized

18

damage is induced in the structure, these distinct feature components are sensed by the neighboring transducers. Extracting the featured components with suitable signal processing techniques is a major task in SHM. In this research, the Matching Pursuit Decomposition (MPD) is used to characterize the influence of delamination on the structural response.

3.1 Matching Pursuit Decomposition

The MPD is an iterative nonlinear algorithm that decomposes any signal into a linear expansion of waveforms that belong to a redundant dictionary. The signal must be expanded into waveforms whose TFR properties are adapted to its local structures. Thus, a modified version of the MPD uses a dictionary that is formed using TFR atoms matched to the analysis signal. If $d(t)$ is the basic TFR atom, α is the dilation or scaling factor, β is the translation factor and κ is the modulation factor, then n^{th} dictionary element $d_n(t)$, $n=1,...,N$, is formed by changing α, β, κ from the following as:

$$d_n(t) = \frac{1}{\sqrt{\alpha_n}} d\left(\frac{t - \beta_n}{\alpha_n}\right) e^{j2\pi\kappa_n t} \tag{29}$$

where n is the total number of dictionary elements. The redundant dictionary covers the entire TF plane, spanned by these time-scaled, time-shifted and frequency-shifted atoms. The objective of the MPD is to decompose a signal $x(t)$ as a linear expansion of waveforms, selected from the dictionary, that best match the TF structure of the signal. This decomposition is done by successive approximations of $x(t)$ with orthogonal projections on dictionary elements and is thus iterative in nature. The signal $x(t)$ is first decomposed as $x(t) = a^1 d_{bm}^1(t) + r^1(t)$, where $r'(t)$ is the residual signal after approximating the signal $x(t)$ with the dictionary element $d_{bm}^1(t)$, $\langle x, d_{bm}^1 \rangle = \int x(t) d_{bm}^1(t) dt$ is the projection of $x(t)$ onto the dictionary element $d_{bm}^1(t)$ and bm

19

represents the best matched dictionary element. This dictionary element corresponds to the signal component with the highest energy. Specifically, $\left|\left\langle x,d_{bm}^1\right\rangle\right| = \max_n\left|\left\langle x,d_n\right\rangle\right|$. After the kth iteration,

$$r^k(t) = \alpha^k d_{bm}^k(t) + r^{k-1}(t), \qquad \alpha^k = \left\langle r^k, d_{bm}^k\right\rangle \tag{30}$$

where $d_{bm}^k(t)$ is the chosen dictionary element that best matches the residual $r^k(t)$ which is given by $r^k(t) = r^{k-1}(t) - \alpha^{k-1}d_{bm}^{k-1}(t)$. In practice, a maximum number of iterations and an acceptable small residue energy compared to the data energy are used as stopping criteria to the algorithm. After K iterations, the decomposed signal is given by

$$x(t) = \sum_{k=1}^{K} \alpha^k d_{bm}^k(t) + r^{k+1}(t) \tag{31}$$

For damage quantification, both simulations and experiments were conducted to obtain the response of a 16 ply 0/90 Gr/Ep composite plate with surface bonded actuators subjected to forced excitation. The investigated damages are 1.5cm×5cm, 3cm×5cm and 4.5cm×5cm delaminations, introduced at different interfaces from the midplane (Fig.17).
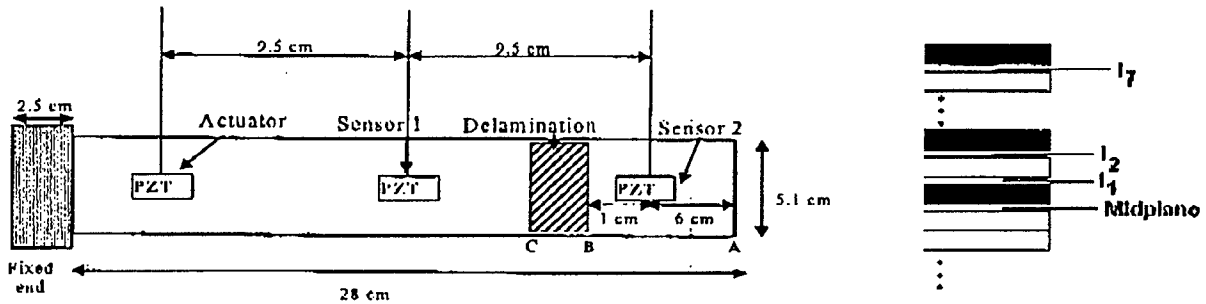

Fig.17. Experimental Setup with Structural Dimensions and Interfaces

In the first set of experiments, a 4.5 cycle tone burst signal with a central frequency of 8 KHz, was used as the excitation signal, sampled at 1MHz. The objective is to quantify the delamination, by decomposing the disturbed signal in terms of wave-based dictionary elements

and time-of-flight analysis of these individual components to determine the location and size of delamination. The basic atom of the MPD is a Gaussian enveloped chirped sinusoid and the dictionary consists of elements which are the time-scaled, time-shifted and amplitude modulated version of the basic atom. This atom was chosen because it satisfies the Lamb Wave modes. Figure 19 shows a typical example of a disturbed signal overlapped with the modeled signal and also the extracted components after decomposition. The sum of the individual components would represent the modeled data. Figure 20 shows a good correlation in the spectrogram TFR of the original and modeled data of sensor-1 (Fig.17).
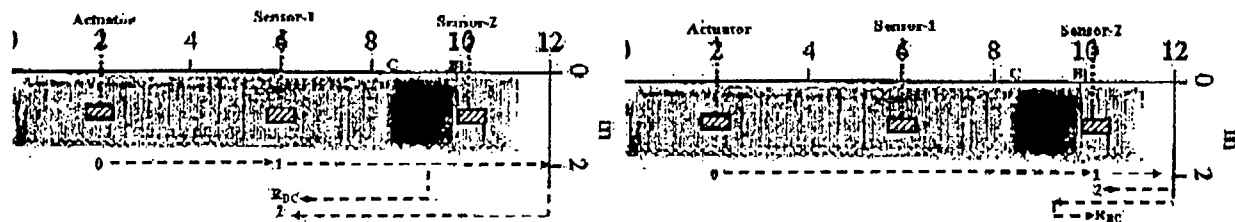

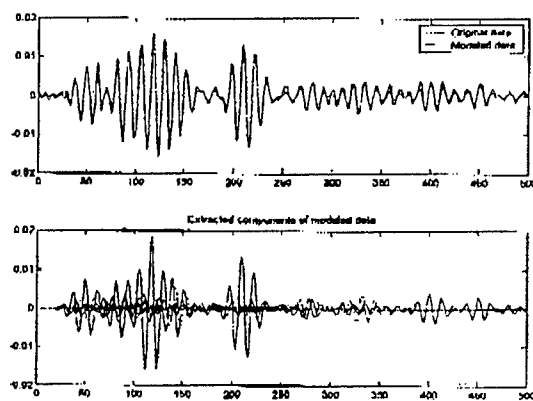Fig.18. Wave Reflections for Sensor-1 (Left) and Sensor-2 (Right)

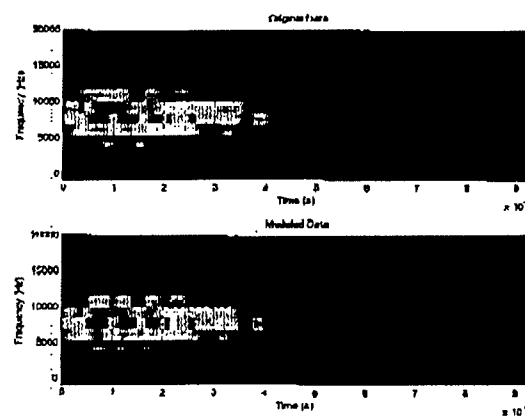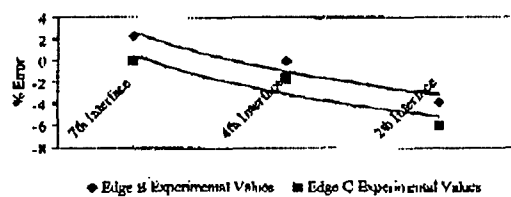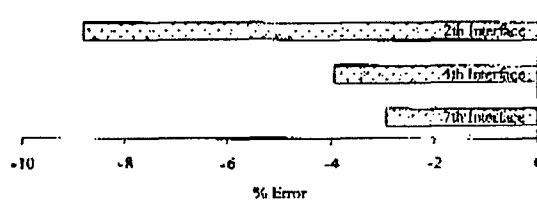Fig.19. Original & Modeled Data

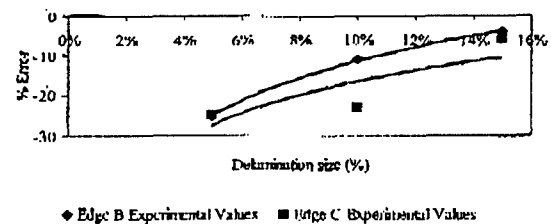Fig.20. TFR of Original & Modeled Data

The time-of-flight information of these individual components is used to determine the location and size of the delamination. The triangulation algorithm is based on the expected wave reflections from the damage and plate edges as demonstrated in Fig.18. Triangulation of rectangular delamination means the detection of the edges (B & C; Fig. 17) of the inclusion. Figure 21 (a) shows the trend of the error to predict the edges when a same size delamination is moved from midplane to near surface. Figure 21 (b) shows the error to estimate the size

◆ Edge B Experimental Values ■ Edge C Experimental Values

(a)

◆ Edge B Experimental Values ■ Edge C Experimental Values

(c)

% Error

(b)

Fig.21. (a): Error in 'Delamination Edge' Detection (%)
Vs. Variation of delamination Interfaces (Z-location)
(b): Error in 'Delamination size' Detection (%) Vs.
Variation of Delamination Interfaces (Z-location)
Y-axis: Error (%), X-axis: 2nd, 4th and 7th Interfaces
(Fixed Delamination Size: 15%)
(c): Error in 'Delamination Edge' Detection (%)
Vs.Variation in delamination size (Delamination fixed at
-2nd Interfaces)
Y-axis: Error, X-axis: Delamination size (%)

delamination based on the fact that delamination is moved from midplane to near surface. Figure 21 (c) shows a similar trend when different sized damages are detected in the 2nd interface.

The second set of experiments was to demonstrate the applicability of the MPD to analyze the vibration attributes of delamination and the influence of 'through-thickness' location and size of the delamination on the structural response under forced excitation. A 8 KHz sinusoidal wave packet has been used as the excitation signal. The basic atom is chosen to be a sinusoidal signal with time duration $0.6\mu s$. The MPD was formed by frequency shifting this basic sinusoid from 2 KHz to 40 KHz, with a resolution of 200 Hz. The dictionary elements were also allowed to be scaled and shifted in time. The comparison of the percentage energy contribution

for the extracted frequency components with the delaminations located at the 2nd interface is shown in Fig.22. In this context, it is important to note that the larger delamination has significant superharmonic components whereas the smaller delamination has subharmonic components with a dominant contribution. A comparative study of the extracted energy components for different delamination sizes, plotted for the normalized frequency scale, is shown in Fig. 22. The normalized frequency scale is obtained by dividing the total frequency range by the excitation frequency (f). As seen from Fig.22., under the influence of sinusoidal pulses, larger delamination toward the midplane acts as a "closing crack" thus giving rise to superharmonic components whereas when the delamination size gets smaller it acts more like a "partially closed crack" giving rise to dominant subharmonic components at the output. These nonlinear effects are more prominent if the delamination is closer to the midplane. This is probably because in such cases the delamination acts more like a perfect "breathing" discontinuity, as it interacts with the excitation signal. Figure 23 shows a similar comparison for a 4.5cm×5cm delamination located at different ply interfaces. As the same size delamination moves closer to the surface, the energy contribution of the principle excitation frequency decreases when compared to delaminations closer to midplane. Near surface delaminations also do not encourage the breathing phenomena. Moreover in the wave based technique, using piezoelectric transducers, local changes are realized while propagating through the structure. Hence the energy dissipation is much higher for near surface delaminations compared to other cases. These phenomena can be well-demonstrated from the extracted frequency components and their corresponding energy contributions, using the MPD technique.
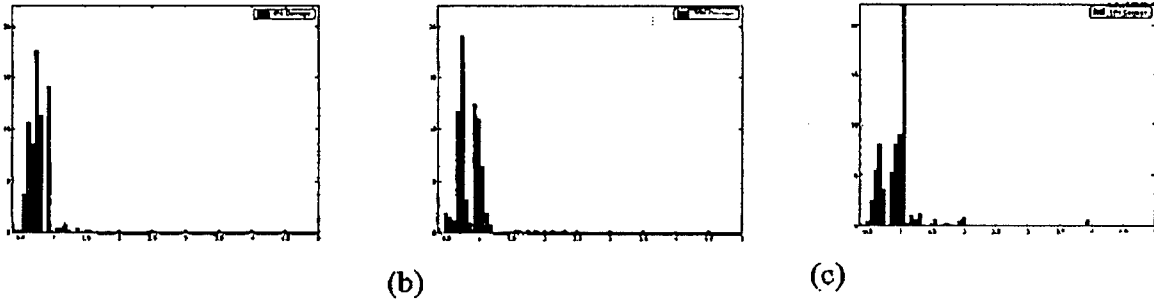
(a) (b) (c)

Fig.22. Extracted frequency components for damaged data, X-axis: Normalized frequency scale, Y-axis: Contribution in extracted energy (%), Frequency of excitation: 8000 Hz, Damage details: Fig.6 (a) 5% Delamination, Fig.6 (b) 10% Delamination, Fig.6 (c) 15% Delamination, at 2nd interface.
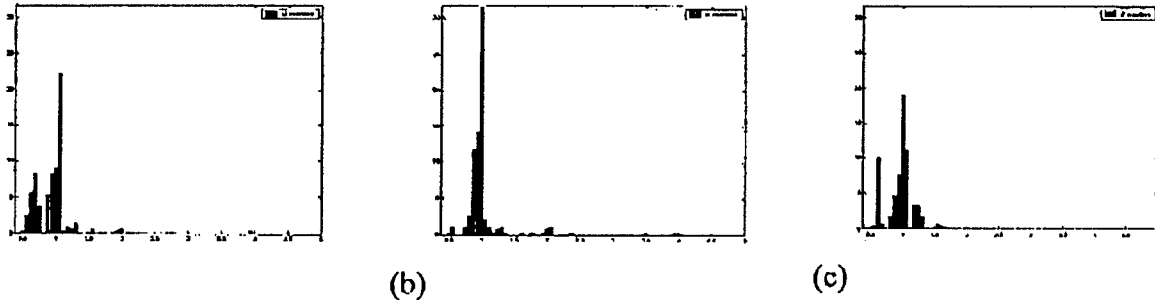

(a) (b) (c)

Fig.23. Comparison of extracted frequency components for damaged data, X-axis: Normalized frequency scale, Y-axis: Contribution in extracted energy (%), Frequency of excitation: 8000 Hz, Damage details: 15% Delamination at Fig.7 (a) 2nd, Fig.7 (b) 4th, Fig.7(c) 7th Interface.

3.2 Matching Pursuit with Adaptive Dictionary

As illustrated earlier, the matching pursuit decomposition is a method for the accurate decomposition of waveforms into linear expansions of elementary functions (or atoms). The resulting decomposition reveals the waveform's structure. This information is used to distinguish signals from healthy and damaged structures. However, if the waveform structure is not well known, there is a need for the MPD to use a comprehensive dictionary to guarantee an accurate decomposition of the waveform. The drawback of the matching pursuit decomposition is that, in the decomposition process, it performs an exhaustive search over a large dictionary of elementary functions. This search is necessary since in most cases the structure of the waveform is not known. For real applications, this results in a large computational burden and a need of large processing power.

24

A method to avoid the exhaustive search over a large dictionary is to identify the atoms that are suitable for the decomposition of a waveform using Monte Carlo sampling. The Monte Carlo Sampling Matching Pursuit Decomposition (MCSMPD) produces a smaller dictionary that is repeatedly adapted to the signal structure and that of its residues, before and during the decomposition process. The MPD is then used to decompose the waveform faster, since it makes use of the smaller dictionary. Furthermore, the dictionary produced by the MCSMPD can contain atoms that are not restricted in a grid in the time, frequency and scale plane, as the MPD dictionary is. This can result to higher decomposition accuracy.

For the decomposition of a given waveform, a dictionary of time-shifted, frequency-shifted and scaled Gaussian enveloped chirped sinusoid atoms are chosen so as to satisfy the Lamb Wave modes generated in the structure. Therefore, the state vector to be estimated has three partitions, each representing the aforementioned atom components. Each of the partitions $l = 1,....L$ evolves according to

$$y_{l,i} = y_{l,i} + \upsilon \tag{32}$$

with $i, i = 1,...,I$, being the iteration step of the particle filter and v being a uniformly distributed noise term that takes values in a relatively small range, that differs for each of the partitions. In the initialization subroutine $i = 1$ and the term $y_{l,i-1}$ is set to zero. Moreover, the noise term ranges from the minimum to the maximum values for each of the partitions that are the same as the ones used for the three respective components of the dictionary used in the regular MP algorithm. This method propagates partitions independently according to a uniform distribution $q(y_{l,i}|y_{l,i-1})$ for each partition l. Where possible, it evaluates their effectiveness in characterizing waveform components individually using a partition weight function that is described in this section. This method is the independent partition method of propagating

partitions that removes the limitations imposed by the increase in the dimensionality of the state vector. The multitarget state vector is expressed in terms of the state vectors of each target as

$$Y_i = \left[y_{1,i}^T y_{2,i}^T ... y_{L,i}^T \right]^T \tag{33}$$

where x^T denotes the transpose of x.

Note that, as each of the particles of the particle filter corresponds to an atom in the dictionary, particles are referred as atoms. If applicable, each proposed partition l of atom $\tilde{y}_{l,k}^n$ is weighed with a partition weighing function, $\tilde{b}_{l,i}^n \propto g_l\left(\tilde{y}_{l,i}^n\right)$. The function $g_l\left(\tilde{y}_{l,i}^n\right)$ is chosen such that it bears information on the specific signal structure that is represented by the specific partition. In this application the time shifts may be weighed with a function that is proportional to the instantaneous energy of the signal at each proposed time. For the frequency shift a weight function is used that is proportional to the Welch periodogram. The partition weight distribution of each partition $\left\{\tilde{b}_{l,i}^n\right\}_{n=1}^N$ normalized and an index j_n' is sampled from the resulting distribution with replacement. The resulting selected partition has the value $y_{l,i}^{n'} = \tilde{y}_{l,i}^{j_n'}$ and bias $b_{l,i}^{n'} = \tilde{b}_{l,i}^{j_n'}$.

For the partitions that are not weighed and sampled, we set $b_{l,i}^{n'} = 1$. The partitions are combined to form atoms $y_i^n = \left[y_{1,i}^n ... y_{L,i}^n\right]$. In the particle weight calculation the inner product $f\left(Y_i^n\right) = \left\langle x, d_{bm}^k \right\rangle$ is included that is a measure of the similarity of the atom to the waveform.

The weight function also takes into account the proposal densities $q\left(y_{l,i} \big| y_{l,i-1}\right)$ and the biases $b_{l,i}^{n'}$. The proposal densities are uniform and with the same variance for each atom.

26

Moreover, each of the partitions is proposed independently. Therefore, the resulting proposal density is equal to $\Pi_l^L q\left(y_{l,i}\middle|y_{l,i-1}\right)$ and when evaluated at each of the atoms it produces equal values for all atoms. Therefore, this factor may be omitted from the weight function that is evaluated up to proportionality. The resulting weights are calculated as: $w_i^n \propto w_{i-1}^n \dfrac{f\left(v_i^n\right)}{\Pi_l^L\left(b_{l,i}\right)}$.

The distribution of $\left\{w_i^n\right\}_{n=1}^N$ is normalized and particles are resembled from this distribution. The steps of this algorithm are described in Table 1.

Table 1 PFMPD algorithm

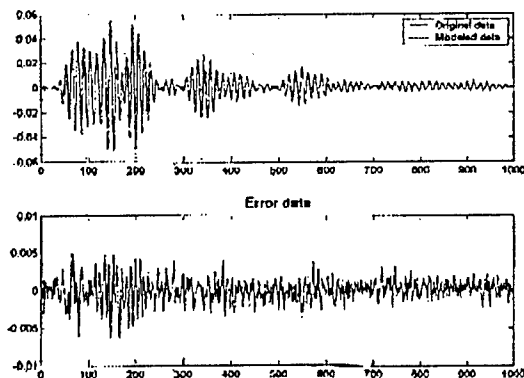| |
|---|
| •   Initialization Subroutine |
| •   Update Subroutine- Repeat M times |
| •   MPD iteration |
| •   If $Rp_k - Rp_{k-1} < .05$ And $Rp_k - Rp_{k-2} > .05$ |
| - Update Subroutine-Repeat M times |
| •   If $Rp_k - Rp_{k-2} > .05$ |
| - Initialization Subroutine |
| - Update Subroutine-Repeat M times |
| •   GOTO MPD iteration |
| •   If $Rp_k < 0.1$ OR $k > 500$ END |

Fig 24. Modeled signal with MPD for Sensor-1 (top) and residual (bottom).
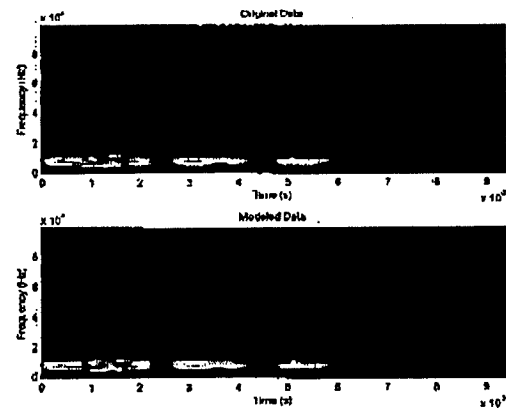

Fig.25. TFR of original and MPD generated modeled signal.
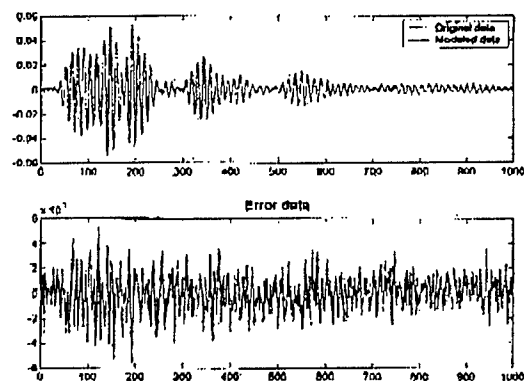

Fig 26. Modeled signal with PFMPD for Sensor-1 (top) generated and residual (bottom).
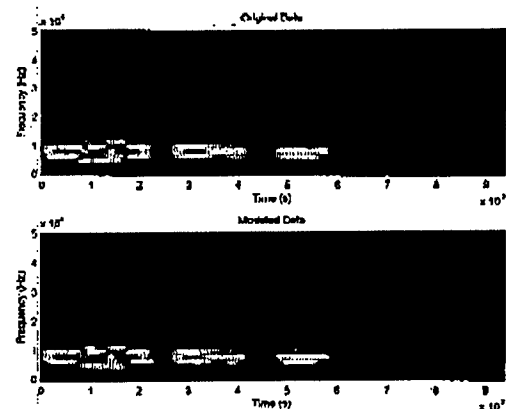
Fig.27. TFR of original and PFMPD modeled signal.

In this analysis Gaussian enveloped chirped sinusoid has been chosen as the basic atom and the dictionary consists of elements which are the time-scaled, time-shifted and amplitude modulated version of the basic atom. For damage quantification, experiments were conducted to obtain the response of a 16 ply 0/90 Gr/Ep composite plate with surface bonded actuators subjected to forced excitation (Fig. 17). The investigated damages are notches, saw-cut, drilled holes, impact and delamination of 4.5cmx5cm introduced at the 4th interfaces from the midplane. In this experiment, a 4.5 cycle tone burst signal with a central frequency of 8 KHz, was used as the excitation signal, and sampled at 1MHz. The ability of the PFMPD algorithm to decompose the same signals with less computational time and without compromising accuracy is demonstrated

in this section. The estimated dictionary is composed of 100 atoms whose range is same as those of the regular MPD dictionary. The dictionary is estimated at every particle filter iteration and adapts to the original waveform and the residues resulting from the MPD. Specifically, the initialization subroutine is used in the beginning of the PFMP algorithm, followed by M= 2 applications of the update subroutine. The MP is used until the fraction of residue R_{pi} at iteration i does not decrease further than 0.05 over one iteration step, when M = 2 update subroutines are used. Moreover, if the fraction of residue does not drop more than 0.05 over two successive MPD iteration steps, the initialization subroutine is used, followed again by M = 2 applications of the update subroutine. The iterations are terminated when either the fraction of residue drops below 0.1 or the maximum time of iterations I = 500 is reached. Figure 24 and 26 shows the same waveform overlapped with the modeled data and also the residue components after decomposition resulting from the MPD and PFMPD respectively. Figure 27 also shows a good correlation in the spectrogram TFR of the original and modeled data of sensor-1.
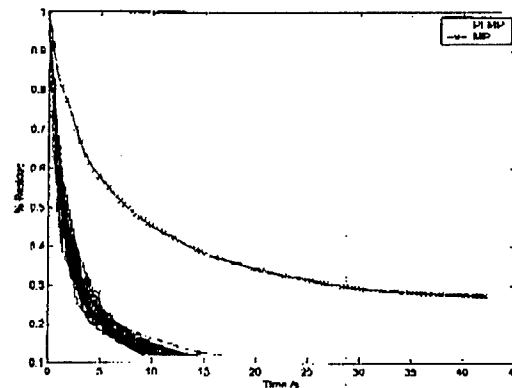
Figure 28 Fraction of residual Vs Computational expense

In Figure 28, it is shown using 50 Monte Carlo simulations, that the PFMPD algorithm with a reduced size dictionary decomposes the given waveform with a fraction of residue comparable to the MPD with a non-adaptive dictionary, but with less computational time. This is due to the fact that the PFMPD, although uniformly proposing atom locations within the time-frequency domain, it appropriately weighs the atoms using the structural information of the

waveform to eventually select those atoms that better match the waveform characteristics. Therefore, the PFMPD is especially useful in locating time-frequency locations of the waveform even if those are found sparsely in the time-frequency domain. In Table 2, the damage locations are predicted from experimental data of individual sensors using both MPD and also PFMPD algorithms.

Table 2 Predicted damage information

Damage Type Dimensions in meter	Original location (m) Of damage From free end	Matching Pursuit Decomposition		MPD with Particle Filter	
		Estimated location (m) Sensor-1 Reading	Estimated location (m) Sensor-2 Reading	Estimated location (m) Sensor-1 Reading	Estimated location (m) Sensor-2 Reading
Drilled holes (0.001 dia)	0.075-0.085	0.147144 0.101014	0.13565 0.149489	0.151757 0.137918	0.061842 0.071068
Delamination (0.045x0.05)	0.055-0.10	0.119466 0.087175	0.094133 0.098746 0.112585	0.151757 0.147144 0.124079	0.061842 0.066455 0.095681
Notch (0.02)	0.07-0.09	0.124079	0.112585 0.117198 0.144876	0.137918 0.133305	0.061842 0.066455 0.071068
Saw-cut (0.02)	0.085	0.114853 0.101014 0.087175	0.080294 0.084907	0.114853 0.101014 0.082562	0.075681 0.080294 0.080294

The reason that sensor-2 provides a better information on the damage location for both MPD and PFMPD, is due to the fact that it experiences a more significant change in the received waveform for damaged and healthy cases when compared to the other sensor. Moreover it is important to note that for certain damages there are multiple entries of predicted damage locations under each sensor depending on reflection components. From the results, it can be observed that the locations of the damages estimated by the PFMPD are closer to the true values that those

obtained by the MPD. This is because the PFMPD is able to propose atoms in continuous locations on the time frequency plane, in contrast to the MPD that is confined only on discrete points. This enables the atoms to more closely represent the waveform at hand.

4. Detection and Classification of Damage Signatures using Support Vectors Machines

The basic idea of classification is to assign any previously unseen pattern of a new point to the predefined class with a closer pattern. There are several techniques to characterize the similarity measures of any given pattern. One way to achieve this is to construct a decision boundary based on the training dataset or the predefined classes and thereafter check the orientation of the given test point with respect to the reference boundary.

An automated method of classifying sensor signals collected from different types of damage coupons to enable the detection and diagnosis of damage on composite structures has been described using Support Vector Machines (SVMs), which are an advanced classification method from the field of machine learning. Figure 29 represents a typical architecture of Support Vector Machines. The use of a special type of support vector machine known as the one-class SVMs has been demonstrated as a pattern recognition tool for automatic anomaly detection and diagnosis on structures made from Carbon Fiber Reinforced Composite (CFRC) materials.
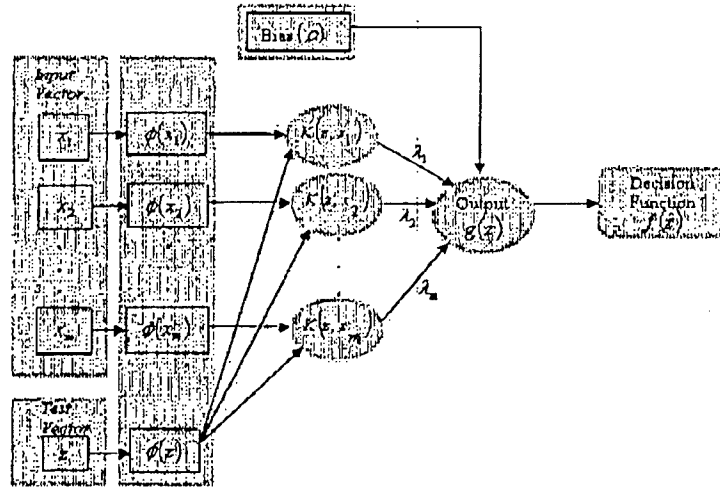
Figure 29 Basic architecture of Support Vector Machines (SVMs)

4.1 One-Class SVMs based Classifier

The Support Vector Machine (SVM) provides non-linear approximations by mapping the input vectors into high dimensional feature spaces where a separating hyperplane is constructed. The idea behind this method is to map the n- dimensional vectors x of the input space X into a high- dimensional (possibly infinite dimensional) feature space. In this research, the input data is mapped into an infinite-dimensional feature space using a Radial Basis Function (RBF) kernel (Eq. 34). The dot product in the feature map (ϕ) is implicitly computed by evaluating the simple kernel (K), thus avoiding the explicit calculation of the feature map.

$$K(x_i, x_j) = <\phi(x_i), \phi(x_j)> = \exp\left(-\frac{\|x_i - x_j\|^2}{2\sigma^2}\right)$$
(34)

One class SVM, proposed by Schölkopf et al, belongs to a unique group of the SVM family where the training input vectors belong to one-class, i.e., the class representative of normal or nominal system behavior. The objective is to map the data into the feature space corresponding

32

to the kernel and thereafter constructing the optimal hyperplane to separate the featured vectors from the origin with maximum margin. All nominal points lie 'above' the optimal hyperplane, and it is assumed that all future nominal behavior will lie in the same region. The algorithm returns a decision function $f(x)$ that evaluates for every new data point (x) to determine which side of the hyperplane it falls on in feature space. Figure 2 represents the schematic overview of the one-class SVM and its parameters. The maximum separation between the origin and the data point is obtained by solving the quadratic problem (Eq. 35). When this algorithm is applied to new data, the decision function is used to determine whether or not the data points lie above or below the hyperplane. Points that fall above the plane (away from the origin) are called, nominal, and other points are called anomalous.
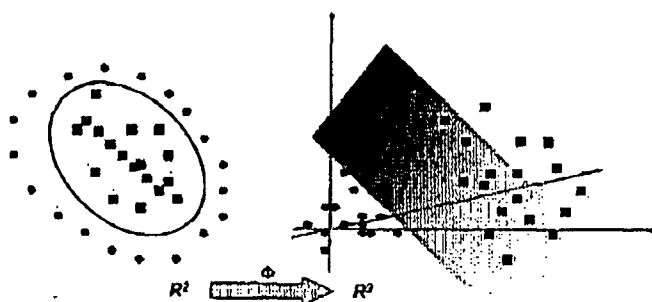
Figure 30 Illustration of higher dimensional mapping for liner separation.

Figure 31 Geometric interpretation of optimal hyperplane construction for two-dimensional case.

$$\min_{w,\rho,\xi,b} \frac{1}{2}\langle w,w\rangle + \frac{1}{l\nu}\sum_{i=1}^{l}\xi_i - \rho \qquad (35)$$

subject to $\langle w,\phi(x)\rangle \geq \rho - \xi_i, \xi_i \geq 0$, for $\nu \in [0,1]$
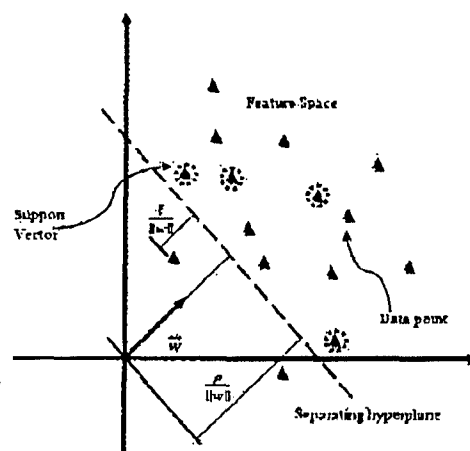
where ν represents the upper bound on the fraction of the training error, ξ is the non-zero slack variable and ρ being the offset (Fig. 31). The target function in the dual problem can be written as,

$$\min_{\alpha} \frac{1}{2} \sum_{i,j} \alpha_i \alpha_j K(x_i, x_j) \tag{36}$$

subject to $0 \leq \alpha_i \leq \frac{1}{l\nu}, \sum \alpha_i = 1$

where α_i represents the Lagrange's multiplier. The parameter ρ can be recovered for values of α_i that satisfies the given constraints with equality sign in Eq. (38) and the values of $\phi(x_i)$ for the corresponding non-zero Lagrange's multipliers (α_i) are termed as support vectors. The obtained α_i and $\phi(x_i)$ must satisfy the equation for the offset, expressed as,

$$\rho = \sum_j \alpha_j K(x_i, x_j) \tag{37}$$

The decision function for a given test vector $\phi(y)$ can be expressed in terms of the kernel as,

$$f(y) = sign\left(\sum_{i-1}^{l} \alpha_i K(x_i, x_j) - \rho \right) \tag{38}$$

For the training data, the decision function takes the value of $+1$ capturing most of the data points and -1 elsewhere. Once the dual problem (Eq. 36) is solved to obtain the support vectors, the optimal hyperplane is constructed in the feature space. For a new test point, the decision function evaluates which side of the hyperplane the given test point falls into, using Eq. 38.

4.2 One-Class SVMs: Detecting Unusual Patterns

In structural health monitoring sensor signals are analyzed to locate and estimate the severity of defect. It is an established fact that the presence of damage introduces additional nonlinearities in the medium. Presence of damage introduces these attributes in terms of undesired attenuation, reflection components, multiple harmonics and high frequency burst signals. In this section, the applicability of One-Class SVMs to detect unusual patterns in signals has been illustrated using two test cases. Figure 32 represents a simulated sensor signal for a healthy structure. The presence of the damage has been represented by introducing additional attenuation, reflections, multiple harmonic components and high frequency burst, superimposed on the resultant wave. In addition a random noise $(w(n))$ has been introduced to take into account environmental and experimental uncertainties. Here $w(n) = \sqrt{X} * random(N,1)$ is a random variable of N realizations and variance X.
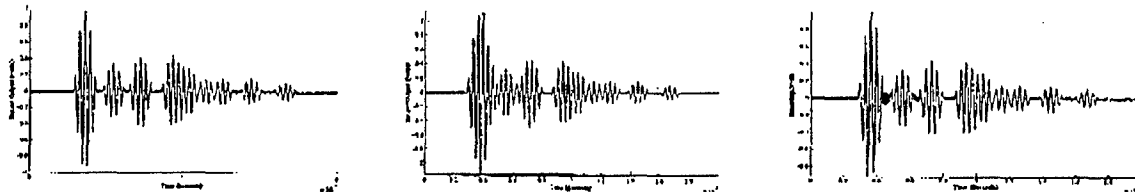
Figure 32 Sensor signal (healthy). Figure 33 Signal with reflections. Figure 34 Signal with high frequency burst.

In Fig. (33) and (34), the signal represents the sensor response of two damage cases with additional reflection components and high frequency burst wave respectively. In both the cases two additional components are introduced at 354th and 585th sample points. The preprocessing of the simulated signal has been done using time-embedded method. In the current analysis, for each time domain data (of 2000 sample points), an 11dimensional state vector is obtained using time delay $\tau = 1$ and embedding dimension $N = 11$. The One-Class SVMs has been trained with the 11 dimensional input vectors from healthy samples and based on the training parameters; the

algorithm constructs the optimal hyperplane. Thereafter the 11 dimensional input vectors corresponding to each damaged case have been tested and the corresponding labels of each data points are checked. It has been observed that majority of the unusual patterns in the signal from the defective cases has been labeled as unseen data or outliers.

Figure (35) represents the plot corresponding to the analysis for the damaged case with additional reflections. The plots corresponding to Fig. (35-a) and (35-b) represents the resultant sensor signal from damaged state and the reflected components from the damage respectively. The predicted outliers are shown as peaks in Fig. 35(c). Figure (36) represents a similar analysis for the damage case with high frequency burst signals. In this context it is important to note that apart from the true predictions, the outcome shows the presence of some false peaks which is basically results due to the presence of the random noise and the nature of the input features provided to the detection algorithm. The performance of the detection system to predict the presence of the additional reflections components has been evaluated with different levels of noise. The confusion matrix has been constructed based on the outcome of the One Class SVMs algorithm. Figure (37) shows the trend of probability of false alarm with different noise level.
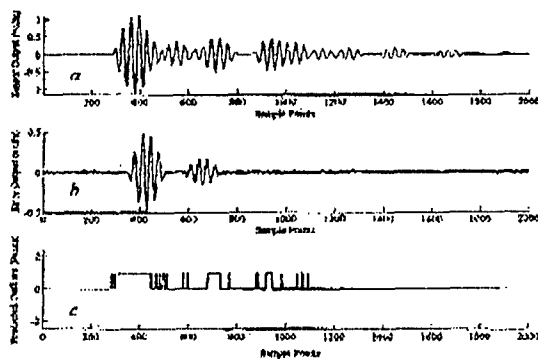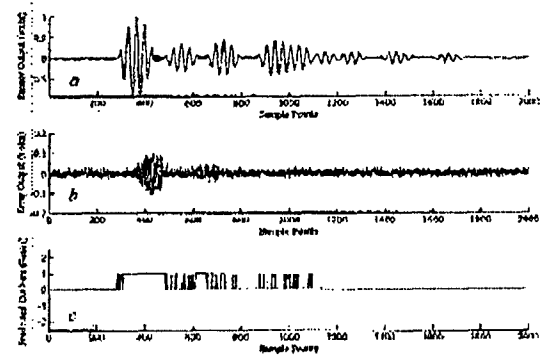

Figure 35 Predicted outliers (additional reflections). Figure 36 Predicted outliers (high frequency burst components).
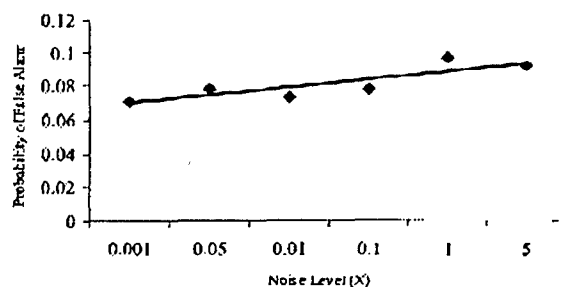
36

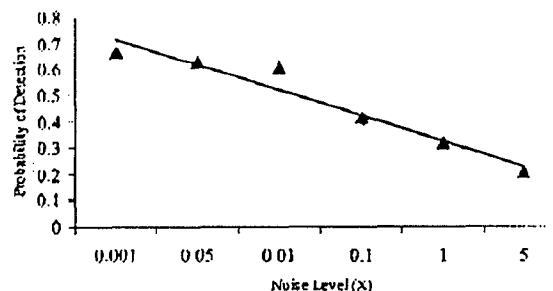Figure 37 Probability of False Alarm Vs. Noise level   Figure 38 Probability of Detection Vs Noise level.

Figure (38) shows a similar plot showing the trend of probability of detection with different noise level. A careful observation reveals that with increasing noise level, the probability of false alarm tends to increase whereas the probability of detections maintains a steady decay as expected. However the sharp fall in Fig. (38) indicates that the probability of detection gets heavily influenced with increasing noise level and thus deteriorates the accuracy of the detection system.

4.3 Classifying Damage Patterns in Integrated Diagnostics

In this section, the use of SVMs to investigate the vibration signatures of damages in composites has been demonstrated under various test applications. The normal (zero-state) and abnormal attributes are extracted from the measured data of a structure and are further analyzed to characterize various states of the system. Once the diagnostic procedure is trained, subsequent test data can be examined to see if the features deviated from the normal behavior have significant similarity with certain abnormal attributes of the system. The goal is to extract and classify the signature characteristics due to the presence of various types of defects in composite structures so that the status of the structure can be ascertained.

For damage quantification, experiments were conducted to obtain the response of a 16 ply 0/90 Graphite/Epoxy composite plate with surface bonded actuators subjected to forced excitation as shown in Fig. 17. The investigated damages (4 categories) are notches, saw-cut,

37

drilled holes and delamination of 4.5cmx5cm introduced at the 4th interfaces from the midplane. The fifth set of data belongs to the healthy group which is used as a reference data for comparison. In the first set of experiments, a 4.5 cycle tone burst signal with a central frequency of 8 KHz, was used as the excitation signal, and sampled at 100 KHz. To take into account the material variability, sensor signals were collected from 2 identical coupons of each group, for example 4 sets of measurements conducted on healthy specimen. A minimum of 10 observations were fetched from each transducer across each test bed under the same operating condition to take into account the experimental uncertainties associated with data acquisition. For classification data, the dataset consists of 20 vectors from each sensor for each category of defects. The objective is to classify the sensor signals collected from different test beds to assist in the diagnosis of composite structures be based on the information from the neighboring sensors (sensor-1 and sensor-2 as shown in Fig. 62).

4.4 Time Embedding Approach

The preprocessing has been done using One-class SVMs along with time-embedded method. The applicability of the time-embedding method along with the One-class SVMs to detect the presence of surprising features in structural data has been demonstrated in the previous sections. Here the classification analysis was conducted for a dataset collected from 2 identical coupons of each group to take into account the experimental and material uncertainties associated with data acquisition and manufacture respectively. In this research, for each time domain data (of 800 sample points), a 11dimensional state vector is obtained using $\tau = 1$ and $N = 11$. A minimum of 20 vectors from each sensor for each category of defects were selected from a pool of 40 vectors and the selection was based on the two datasets having the closest distribution. In this effort, a total of total 790 X 4400 dimensional matrices (S) corresponding to 5 defect

38

conditions has been used using time-embedded technique. As mentioned, 50% of the observations related to each condition are used as the training samples and the others as the testing samples.

Table 3 and 4 presents the outcomes (R) using SVMs on the damage classification for sensor-1 and sensor-2 respectively, using a RBF kernel. Here R_{ij} represents the correct classification rate of a dataset from any j^{th} category (represents each column) when trained with a dataset from i^{th} category (represents each row). In the current analysis, the ν is set to 0.05 and the optimal σ is being calculated for each training set. Once the matrix (R) is calculated, the selection criteria that two groups of signals belong to the same class is true when R_{ij} and R_{ji} closely matches with higher classification rate i.e. $R_{ij} \cong R_{ji}$. When One-Class SVMs is trained with j^{th} category dataset, most of the jth category feature points lie on one side of the hyperplane but majority of the ith category feature points (from test dataset) may or may not lie on the same side of the hyperplane. In case the category feature points don't lie on the same side, then they are from different classes. However if they do, then it would be necessary to cross check if they both lie on the same side of the hyperplane, when the SVM is trained with category dataset instead. The geometrical interpretation for the selection criteria means that the two hyperplanes constructed individually by i^{th} category and j^{th} category dataset has to be very similar such that majority feature points from both the categories lie on the same side irrespective of the hyperplane constructed. In the present analysis, the selection criteria is set as $\|R_{ij} - R_{ji}\| \leq 0.05(1 - \gamma)$, which means that to belong to the same class the absolute difference of the correct classification rate obtained from two sets of data must be less than or equal to 5% of the maximum classification rate. Once the R matrix is obtained, a new matrix Q_{ij}^k is formed for

the kth sensor, such that the following criteria hold,

$$If, \left\| R_{ij} - R_{ji} \right\| \leq 0.05(1 - \gamma)$$

$$Q_{ij}^{k} = Q_{ji}^{k} = 1$$
$$Else \qquad\qquad\qquad (39)$$
$$Q_{ij}^{k} = Q_{ji}^{k} = 0$$

For each sensor-1 (*s1*) and sensor-2 (*s2*), the Q_{ij}^{k} is evaluated and finally compared to obtain M, where

$$M = Q^{s1} I Q^{s2} \qquad\qquad\qquad (40)$$

The matrix (M) represents the final outcome of the classifier based on the mutual information of the sensor pairs and can infer that i^{th} category and j^{th} category dataset belong to the same group, if $M_{ij} = M_{ji} = 1$. The One-class SVMs classifiers successfully classified all the defect states, and are shown in Table 5. The proposed technique provides a One-Class based classification technique using feature vectors extracted applying the time-embedding method directly to the sensor response but not the difference output. It has been demonstrated that the developed analysis based on mutual information from multiple sensor is an effective way of minimizing the possibility of false classification, when coupled with a selection criterion.

$\nu -0.05$ σ		TRC1 (test)	TRC2 (test)	TRC3 (test))	TRC4 (test)	TRC5 (test)	TEC1 (test)	TEC2 (test)	TEC3 (test)	TEC4 (test)	TEC5 (test)
0.055	TRC1 (train)	0.9544	0.6873	0.8683	0.6227	0.8101	0.7620	0.6278	0.8075	0.4949	0.7202
0.16	TRC2 (train)	0.9594	0.9506	0.8468	0.7860	0.8202	0.9177	0.7683	0.8696	0.7911	0.8202
0.105	TRC3 (train)	0.9164	0.7189	0.9506	0.6519	0.8278	0.8797	0.7012	0.8594	0.6443	0.8240
0.08	TRC4 (train)	0.8468	0.8075	0.8632	0.9531	0.8215	0.9025	0.7025	0.8455	0.6734	0.8139
0.09	TRC5 (train)	0.8797	0.6974	0.9050	0.6607	0.9557	0.8822	0.7025	0.9139	0.5962	0.9038
0.06	TEC1 (train)	0.8012	0.6506	0.8506	0.5379	0.7569	0.9544	0.6924	0.8670	0.6468	0.8278
0.155	TEC2 (train)	0.9126	0.7620	0.8670	0.7924	0.8189	0.9594	0.9531	0.8455	0.7860	0.8215
0.115	TEC3 (train)	0.9038	0.7202	0.8835	0.6835	0.8379	0.9405	0.7303	0.9519	0.6658	0.8303
0.075	TEC4 (train)	0.8822	0.6974	0.8405	0.6645	0.8025	0.8519	0.8063	0.8519	0.9544	0.8050
0.085	TEC5 (train)	0.8278	0.6873	0.9025	0.5784	0.9038	0.8721	0.6797	0.8936	0.6177	0.9544

Table 4: Classification rate (R_{ij} matrix) for sensor-2

$\nu=0.05$ σ		TRC1 (test)	TRC2 (test)	TRC3 (test))	TRC4 (test)	TRC5 (test)	TEC1 (test)	TEC2 (test)	TEC3 (test)	TEC4 (test)	TEC5 (test)
0.115	TRC1 (train)	0.9519	0.9291	0.8949	0.7936	0.9202	0.9240	0.9113	0.8949	0.8012	0.9240
0.08	TRC2 (train)	0.6658	0.9506	0.6215	0.7151	0.6683	0.6379	0.8620	0.6924	0.6582	0.6063
0.1	TRC3 (train)	0.8392	0.8645	0.9531	0.7164	0.8569	0.8341	0.8860	0.8392	0.6734	0.8506
0.1	TRC4 (train)	0.8835	0.9126	0.8075	0.9544	0.8848	0.7987	0.9075	0.7949	0.7379	0.8557
0.12	TRC5 (train)	0.8493	0.8873	0.8670	0.7367	0.9506	0.8873	0.8873	0.8746	0.7215	0.8911
0.115	TEC1 (train)	0.9177	0.9063	0.8962	0.8139	0.9240	0.9531	0.9227	0.8949	0.7974	0.9202
0.08	TEC2 (train)	0.6353	0.8594	0.6886	0.6557	0.6088	0.6594	0.9557	0.6139	0.7126	0.6645
0.095	TEC3 (train)	0.8240	0.8746	0.8341	0.6582	0.8544	0.8519	0.8670	0.9506	0.7101	0.8493
0.11	TEC4 (train)	0.8139	0.9088	0.7962	0.7582	0.8721	0.8987	0.9202	0.8215	0.9557	0.8848
0.12	TEC5 (train)	0.8417	0.8873	0.8734	0.7265	0.8911	0.8683	0.8873	0.8645	0.7341	0.9531

$\vdots$

$\vdots$

$\vdots$

$\vdots$

Table 5: Outcome of the classifier

(case-3)

Nu=0.95		TRC1 (test)	TRC2 (test)	TRC3 (test))	TRC4 (test)	TRC5 (test)	TEC1 (test)	TEC2 (test)	TEC3 (test)	TEC4 (test)	TEC5 (test)
0.07	TRC1 (train)	1	0	0	0	0	1	0	0	0	0
0.06	TRC2 (train)	0	1	0	0	0	0	1	0	0	0
0.085	TRC3 (train)	0	0	1	0	0	0	0	1	0	0
0.07	TRC4 (train)	0	0	0	1	0	0	0	0	1	0
0.08	TRC5 (train)	0	0	0	0	1	0	0	0	0	1
0.075	TEC1 (train)	1	0	0	0	0	1	0	0	0	0
0.045	TEC2 (train)	0	1	0	0	0	0	1	0	0	0
0.05	TEC3 (train)	0	0	1	0	0	0	0	1	0	0
0.075	TEC4 (train)	0	0	0	1	0	0	0	0	1	0
0.08	TEC5 (train)	0	0	0	0	1	0	0	0	0	1

Publications

1. Chattopadhyay, A., Zhou, X., and Das, S., "Behavior of Elastic Wave Propagation in Fiber Reinforced Composite Materials," Journal of Intelligent Material Systems and Structures (accepted), 2004.
2. Chattopadhyay, A., Zhou, X., and Das, S., "Acoustic Based Structural Health Monitoring for Composites Using Optimal Sensor Placement: Analysis and Experiments," Journal of Reinforced Plastics and Composites (accepted), 2004.
3. Chattopadhyay, A., Zhou, X., Miller D.K., and Das, S., "Elastic wave attenuation in composite laminates with cracks," 12th SPIE Annual International symposium on Smart Structures and Materials, San Diego, California, 2005.
4. Chattopadhyay, A., Zhou, X., Papandreou-Suppappola, A., and Das, S., "On the Use of the Matching Pursuit Decomposition Signal Processing Technique for Structural Health Monitoring," 12th SPIE Annual International symposium on Smart Structures and Materials, San Diego, California, 2005.
5. Chattopadhyay, A., Papandreou-Suppappola, A., and Das, S., "A Novel Signal Processing Technique for Damage Detection in Composites," International Conference on Computational & Experimental Engineering & Sciences, Chennai, India, 2005.
6. Chattopadhyay, A., Papandreou-Suppappola, A., and Das, S., "Structural Health Monitoring of Composites using Wave Based Technique and Novel Signal Processing," Condition Monitoring, King's College, Cambridge, United Kingdom, 2005.
7. Chattopadhyay, A., Miller D.K., and Das, S., "Wave scattering analysis of bolted joints," Nondestructive Evaluation and Health Monitoring of Aerospace Materials, Composites, and Civil Infrastructure, Proceedings of the SPIE, San Diego, California, 2006.
8. Chattopadhyay, A., Papandreou-Suppappola, A., Kyriakides, I., and Das, S., "Particle Filter Based Matching Pursuit Decomposition for Damage Quantification in Composite Structures," 47th AIAA/ASME/ASCE/AHS/ASC Structures, Structural Dynamics, and Materials Conference, Newport, Rhode Island, 2006.
9. Chattopadhyay, A., Srivastava, N. A., and Das, S., "Classification of Damage Signatures in Composite Plates using One-Class SVMs," IEEE Aerospace Conference, Big Sky, Montana, 2006. (Accepted)

Honors/Awards

Aditi Chattopadhyay - Elected AIAA Fellow, November 2005

Structural Health Monitoring of Heterogeneous Systems Using Non-contact Pulse Echo Thermography

Principal Investigator: Aditi Chattopadhyay

Department of Mechanical and Aerospace Engineering
Arizona State University
Tempe, AZ 85287-6106

Description of Research Conducted

The thermal wave imaging system (EcoTherm) has been used in the ongoing research activities related to Structural Health Monitoring (SHM) of heterogeneous structural systems. The equipment has been used as a module integrated with the existing generalized framework for the characterization, detection and quantification of damage such as delamination in composite structures. The existing framework comprises experimental procedures, along with developed numerical techniques to characterize damage in laminated composites, using surface bonded and embedded piezoelectric sensors. Experimental techniques comprise the use of non-contact air coupled ultrasonics, laser vibrometry and thermography. The EchoTherm system uses a pulse echo thermal wave to capture 3-D images in real time. A heat pulse is generated by a set of flash lamps and launched on the surface of the composite laminated coupons with embedded delaminations. Once the thermal waves start propagating through the interior plies of the laminated structure, the presence of defects such as delaminations would cause the propagating thermal wave to reflect back because of the difference in the media properties. The system consists of an infra-red camera and associated electronics, which is used to form and store the images of the subsurface defects. In the ongoing research, the thermography system has been used to investigate seeded delamination in composite beams and plates.

A hierarchical wave based approach has been developed for further quantification of and classification of delaminations patterns. In the current effort, a Matching Pursuit Decomposition (MPD) algorithm has been developed for detection and localization of

seeded delamination in composite structures. This has been accomplished by decomposing the signal in terms of wave-based dictionary elements and finally utilizing the time-of-flight information of these individual decomposed components of transient datasets to determine the location and size of the delamination. The performance of the developed diagnostic system with embedded sensing architecture for health monitoring of laminated composite structures has been evaluated against the predictions of the thermal wave imaging system by validating the detection and localization of the delaminations.

Status of Effort

Experiments have been conducted to obtain the response of a composite plate with surface bonded actuators subjected to sinusoidal loading. A 16 ply graphite/epoxy cantilever plate with 0/90 stacking sequence is used. The plate dimensions are: 30.5cm long, 5.1cm wide, 0.00218 cm ply thickness. Thunder PZTs, bonded to the upper surface of the plate, are used as sensors and actuators. Figure 1 demonstrates the placement of sensors and the actuator.
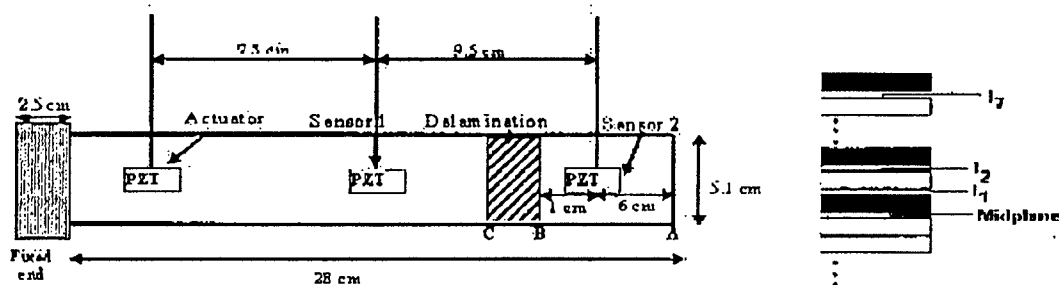

Figure 1 Experimental Setup with Structural Dimensions and Interfaces of composite beam.

The damage is represented by delamination of various sizes, introduced at different interfaces from the midplane as shown in Fig. 1. The investigated damages are of 1.5cm x

5cm, 3cm x 5cm and 4.5cm x 5cm delaminations as shown in Fig. 2. In the current set of experiments, a 4.5 cycle tone burst signal with a central frequency of 8 KHz, was used as the excitation signal, sampled at 1MHz. The objective is to quantify the delamination, by decomposing the disturbed signal in terms of wave-based dictionary elements and time-of-flight analysis of these individual components to determine the location and size of delamination.

4.5 cm X 5 cm delamination at 2nd interface

4.5 cm X 5 cm delamination at 4th interface

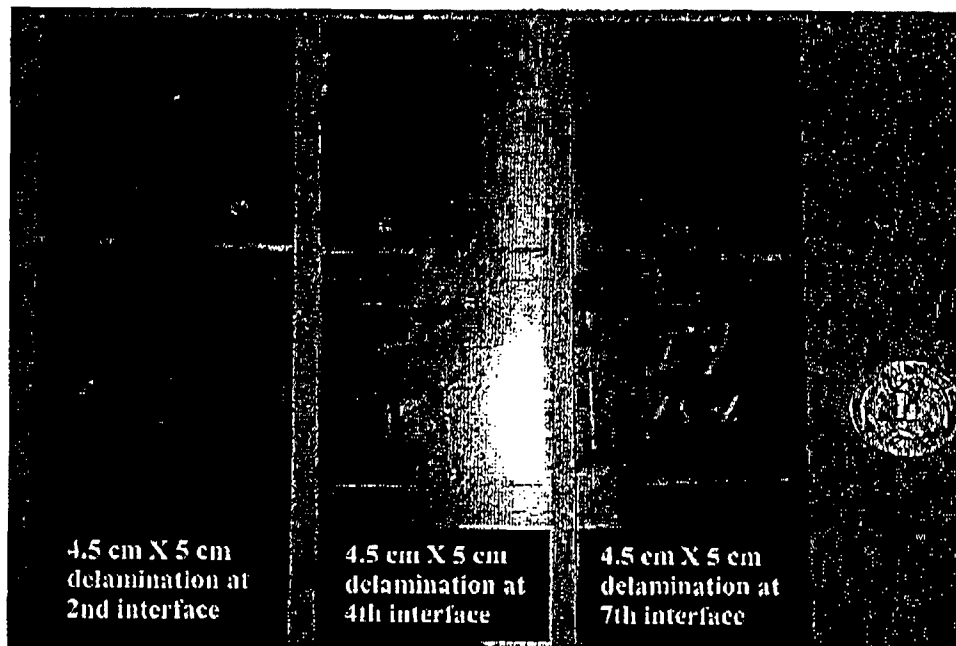4.5 cm X 5 cm delamination at 7th interface

Figure 2 Composite coupons with delaminations.

The time-of-flight information of these individual components is used to determine the location and size of the delamination. The triangulation algorithm is based on the expected wave reflections from the damage and plate edges as demonstrated in Fig. 3 and Fig. 4 for sensor-1 and sensor-2 respectively.
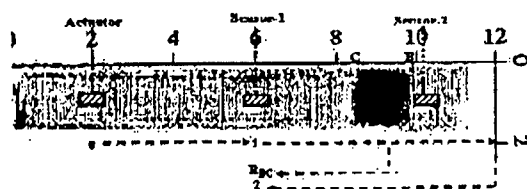
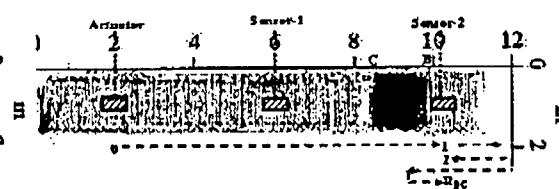Figure 3 Wave Reflections for Sensor-1.   Figure 4 Wave Reflections for Sensor-2.

Triangulation of through-width rectangular delamination implies the detection of the edges (B & C; Fig. 3-4) of the inclusion. The above figure represents the c-scan of the sample plate with a seeded delamination introduced at 4th interface from the mid-plane. Table 1 represents the estimated values, based on the first 5 reflections, for the delamination edges when different sizes of delaminations are moved from midplane to near surface. The values are obtained by applying the triangulation algorithm on the decomposed components obtained from the MPD model.

Table 1 MPD output based on 5 reflections

Delamination Size	Delamination Location	Actual (B)	Actual (C)	Predicted (B)	Predicted (C)
4.5cm×5cm	I_7	0.065	0.116	0.063	0.116
4.5cm×5cm	I_4	0.065	0.116	0.065	0.118
4.5cm×5cm	I_2	0.065	0.116	0.067	0.123
3.0cm×5cm	I_2	0.073	0.103	0.081	0.127
1.5cm×5cm	I_2	0.080	0.097	0.100	0.121

Figure 5-6 represents the C-scan images of some of the test samples used for quantification purpose (Fig.2). The existing ultrasonic testing equipment (SONDA 007 CX) has been used to automatically scan the test samples for the detection and measurement in the attenuation domain to characterize the defect and to analyze the interfaces for possible existing damage. Figure (7-8) represents the thermographic images

of some of the same test samples used for quantification purpose as shown in Fig. 5-6. The existing EcoTherm system has been used to capture the thermal images using a pulse of heat, generated by a set of flash lamps and launched on the surface of the test sample that is being investigated. The c-scan image and thermographic image has been used for validating the existence of defects, including the damage severity and finally compared with these results with those obtained using wave based techniques (table 1).
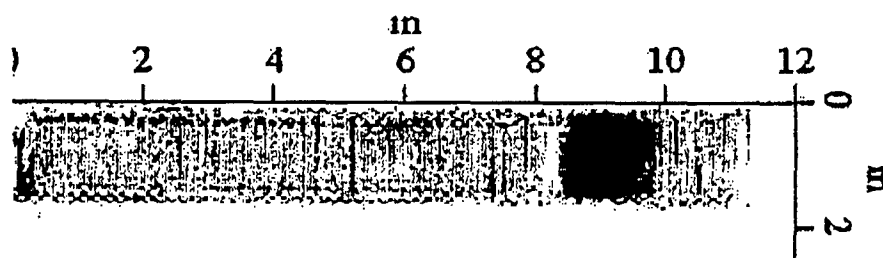

Figure 5 C-scan of composite coupons with delamination (4th interface).
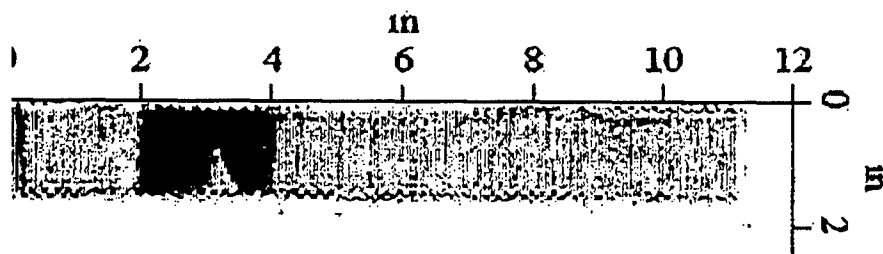

Figure 6 C-scan of composite coupons with delamination (7th interface).

Figure 7 Thermographic image of composite coupons with delamination (4th interface).

Figure 8 Thermographic image of composite coupons with delamination (4th interface).